THE AMERICAN SOCIETY OF MECHANICAL ENGINEERS
345 E. 47th St., New York, N.Y. 10017

98-GT-254

EXPERIMENTAL AND COMPUTATIONAL STUDY OF THE UNSTEADY FLOW IN A 1.5 STAGE AXIAL TURBINE WITH EMPHASIS ON THE SECONDARY FLOW IN THE SECOND STATOR

Ralf E. Walraevens, Heinz E. Gallus
Institut für Strahlantriebe und Turboarbeitsmaschinen
RWTH Aachen
D-52062 Aachen, Germany

and

Alexander R. Jung, Jürgen F. Mayer, Heinz Stetter
Institut für Thermische Strömungsmaschinen und Maschinenlaboratorium
University of Stuttgart
D-70550 Stuttgart, Germany

ABSTRACT

A study of the unsteady flow in an axial flow turbine stage with a second stator blade row is presented. The low aspect ratio blades give way to a highly three-dimensional flow which is dominated by secondary flow structures. Detailed steady and unsteady measurements throughout the machine and unsteady flow simulations which include all blade rows have been carried out. The presented results focus on the second stator flow. Secondary flow structures and their origins are identified and tracked on their way through the passage. The results of the time-dependent secondary velocity vectors as well as flow angles and Mach number distributions as perturbation from the time-mean flow field are shown in cross-flow sections and azimuthal cuts throughout the domain of the second stator. At each location the experimental and numerical results are compared and discussed. A good overall agreement in the time-dependent flow behaviour as well as in the secondary flow structures is stated.

NOMENCLATURE

c	absolute velocity
w	relative velocity
u	circumferential velocity
Ma	Mach number
t	pitch
t	time
y^+	dimensionless wall distance
α	pitchwise flow angle (abs. frame)
β	pitchwise flow angle (rel. frame)
γ	spanwise flow angle
λ	stagger angle
PS, SS	pressure side, suction side
TI	time index
0	first stator inlet
1	rotor inlet
2	rotor exit, second stator inlet
3	second stator exit
loc	local (flow vector)
avg	averaged
uns	unsteady
sec	secondary (flow vector)
$-r$	radially averaged
$-\varphi$	circumferentially averaged
$'$	fluctuation

INTRODUCTION

To improve performance and design of turbomachines currently being developed further understanding of the physical basics is essential. Most of the present analysis and design methods are based on steady aerodynamics. But unsteady flow associated with blade row interaction causes highly three-dimensional flow fields that change periodically with time. It is necessary to check the influence of the periodic unsteadiness on loss generation and extend the design process, taking in account time-dependent flow features.

One most important source of unsteadiness is the relative motion of blade rows. Turbine rotor flow is influenced by the non-uniform exit flow of the first stator and the periodically incoming wakes induced by the upstream stator blades. In addition passage vortices and the tip clearance vortex develop during the flow passes the rotor. The strongly distorted three-dimensional rotor exit flow now enters the passage of the second stator. Entering the passage, rotor wakes and vortices are cut off by the vanes of the second stator. The already unsteady flow has

Presented at the International Gas Turbine & Aeroengine Congress & Exhibition
Stockholm, Sweden — June 2–June 5, 1998

to follow blade curvature thereby inducing the stator passage vortices. All these effects lead to a strongly disturbed, three-dimensional and highly unsteady second stator exit flow. To understand, describe and model these complex phenomena detailed experimental investigations in rotating turbomachines are necessary.

A number of experimental studies have been carried out in recent years. Joslyn et al. (1983) demonstrated that the rotor outlet flow at midspan of a turbine changes remarkably as the rotor interacts periodically with the stator wakes. The three-dimensional flow through a large-scale turbine was measured by Hunter (1982), Sharma et al. (1985) and Joslyn and Dring (1992). They detected considerable variations of flow angles, velocity and pressure distributions for different rotor-stator positions. Binder et al. (1985) measured a sudden increase of turbulence energy when the rotor cuts off the passage vortices of the upstream stator row. Extensive studies of the unsteady rotor flow were carried out by Zeschky and Gallus (1993). They proved that the development of the rotor secondary flow, the rotor wake and the outlet flow angles is strongly influenced by the non-uniform stator exit flow and the periodically unsteady rotor inlet flow respectively. Sharma et al. (1988) showed the impact of unsteadiness on the characteristics of secondary flows in the downstream rotor and stator passages. They proposed a semi-elliptical model to provide improved estimates of losses in the midspan regions of turbine rotors. Morphis and Bindon (1994) described the response of the second stator to the complex tip clearance flow in a 1.5 stage low speed axial turbine. Investigations on the unsteady flow before, within and behind the second stator passage in a 1.5 stage turbine were performed by Yamamoto et al. (1993). A large axial gap between first stator and rotor was installed to minimize the effects of the wakes of the first stator on the rotor inlet flow. Their results indicate that the stator passage and stator exit flow mainly depend on the rotor exit flow and the secondary flow generated within the stator passage.

During the last five years, several computational studies of flow associated with blade row interaction have been carried out e.g. by Hah et al. (1993), Valkov and Tan (1993), Gallus et al. (1994), Dawes (1994), Eulitz et al. (1996), He (1996), and Hall (1997). Looking at the complex pattern of the flow in multi-blade row machines it becomes obvious that a numerical method to accurately predict the time-dependent secondary flow in multi-blade row environment has to account for the three-dimensionality as well as the unsteadiness of the flow. With the recent development of more powerful computers especially of affordable high performance workstations and with the improved and more efficient numerical methods time-accurate flow simulations in turbomachinery stages can be performed with reasonable spatial and temporal resolutions.

The present paper concentrates on the three-dimensional highly unsteady flow conditions behind the rotor, in the passage of the second stator and behind the second stator of a 1.5 stage axial flow turbine. At various locations throughout the domain of the second stator, the experimental and numerical results are presented, compared and discussed. The simulations allow to take a close look even at spaces where it is impossible to get reasonable experimental data wheras the experiments are especially essential to verify the unsteady flow predictions. The results will on one hand provide a better understanding of unsteady flow phenomena but on the other hand they may help to find ways for further improvement of time accurate numerical methods.

EXPERIMENTAL FACILITIES AND TECHNIQUE

Experimental data behind rotor and second stator was acquired in a 1.5-stage axial turbine shown in Fig. 1. For both stators the Traupel profile is used (Utz, 1972). Profile geometry, number of blades and stagger is identical for the first and the second stator. A modified VKI-profile is used for the rotor. The tip clearance is 0.4 mm Both stators and the rotor consist of untwisted blades. Stator vanes are stacked in the trailing edge, rotor blades in the center of gravity. A cross section of the turbine with mid-span velocity triangles and definitions of the flow angles is shown in Fig. 2. The design point of the turbine is at a rotational speed of 3500 rpm. The shaft speed variation was less than 0.2 percent. Total temperature at turbine inlet was maintained in the range of 308 K +/-0.5 K by cooling the supplying air at the compressor outlet. Mach number at inlet was adjusted to Ma=0.11 with an accuracy of about 0.5 percent.

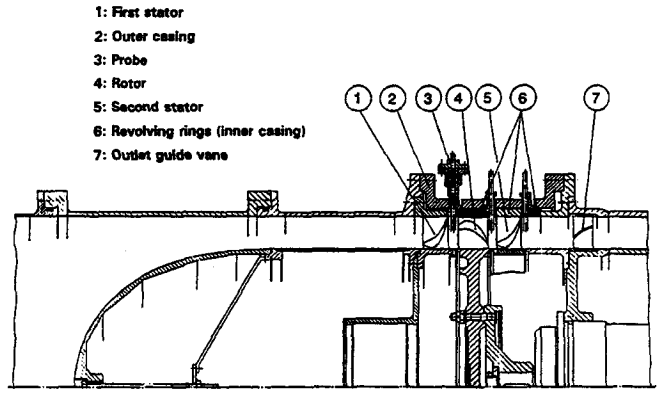

Figure 1: Turbine test facility

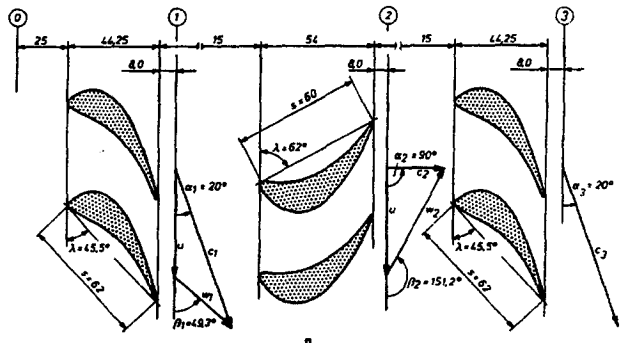

aspect ratio h/s	0.887	0.917	0.887
pitch (midspan) t	47.6 mm	41.8 mm	47.6 mm
blade number	36	41	36
Reynolds number, based on chord and exit velocity	6.8×10^5	4.9×10^5	6.9×10^5
rotational speed	----	3500 rpm	----
tip diameter	600 mm	600 mm	600 mm

Figure 2: Turbine geometry and design data

Time-dependent flow field properties behind rotor and second stator respectively have been measured with a triple-hot-wire probe 8 mm behind the blade rows (station 2 and 3, Fig. 2) The probe was traversed in a radial-circumferential array covering 9 % to 91 % span in the radial direction (20 positions) and one stator vane pitch (17 positions) in the circumferential direction. Measurements within the passage of

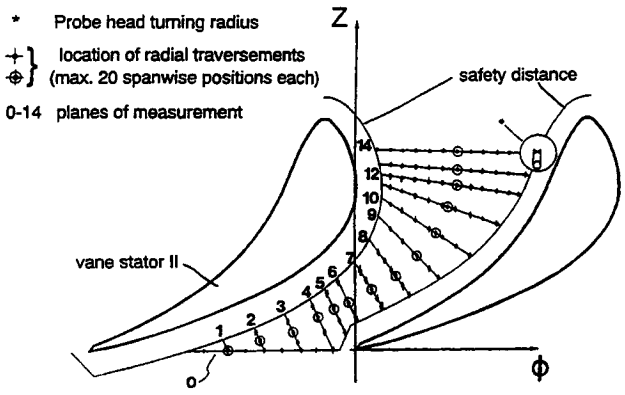

Figure 3: Location of measurements within the second stator passage

the second stator have been carried out with a special, small stemmed triple-hot-wire probe with a diameter of the stem and measuring volume of 1,9 mm. High resolution of the unsteady flow has been achieved by 92 radial traversements at locations shown in Fig. 3. The safety distance (Fig. 3) has been applied to avoid probe damage as well as to minimize interaction between probe and vane surface.

During the test the fluctuating output signal has been stored with a multi-channel tape recorder on usual video cassettes. The trigger signal was recorded at the same time and stored on the tape as well. All devices were controlled by a personal computer which stored also the time-averaged voltages, logged with the voltmeter. This was to calculate steady values of velocity and flow angles which were used to check the quantities during the test.

To evaluate the data stored on tape a multi-channel data acquisition device was connected to the tape recorder. Playing the tape 512 real-time samples were recorded for each of 128 revolutions. This covers about 8 blade passing periods. Using the phase-locked ensemble average method (Gostelow, 1977) the data was reduced and calibrated to 64 different rotor/stator positions along one rotor pitch.

NUMERICAL APPROACH

Flow Solver ITSM3D

The equations solved are the fully three-dimensional, unsteady, Favre-averaged Navier-Stokes equations. They are written for a cylindrical coordinate system that rotates at constant angular velocity, see Jung et al. (1996). The fluid is assumed to behave as an ideal gas with a constant ratio of specific heat capacities. A modified algebraic Baldwin-Lomax model is used to describe the effects of turbulence. The solution method is based on the work of Jameson et al. (1981). An explicit five-stage Runge-Kutta time stepping scheme is used.

In cases of unsteady simulations in which the stator blade count is different from the rotor blade count, a time-inclining method for three dimensions based on the work of Giles (1991) is used in order to model the exact ratio of the blade counts. In this approach, time-transformations are applied to both the stator and the rotor domains and different time steps are used in these domains. In this way simple periodicity conditions can be applied at the boundaries in pitch-wise direction although these boundaries are not periodic in the physical domain. Multiple blade passage can be used to overcome the stabilty limitation of the time-inclination method for the cases in which the difference in the blade counts of the stage is so large that in the time-transformed space the principle of causality would be violated.

At the inlet and exit boundaries as well as at boundaries between two domains in the case of steady-state flow interaction of two blade rows, a non-reflecting post-correction method based on the work of Giles (1988) is applied to prevent spurious reflections from waves that leave the computational domain. Solid surfaces are assumed adiabatic and the no-slip condition is applied. Periodicity in pitch-wise direction is ensured through the use of dummy cells that keep copies of the periodic values such that the points on these boundaries can be treated like interior points.

Block-structured H-type grids in a multi-block topology allow modelling of complex geometries, e. g. blade tip gaps or computational domains consisting of multiple blade passages. At the sliding interfaces between stationary and rotating blade rows the grids are overlapped by one grid cell. An interpolation procedure consistent with the second order spatial accuracy of the numerical scheme is used to interchange the flow variables during every time step of the integration procedure. As the rotor grid moves relative to the stator, the rotation of the rotor is integrated in time in order to track the position of the grid blocks for a time-resolved coupling at the interface regions.

For steady-state calculations a full multi-grid method, local time stepping and implicit residual smoothing can be used to accelerate convergence to a large extent, see Merz et al. (1995). In the case of unsteady calculations a time-consistent multigrid scheme based on the work of He (1996) and an implicit residual averaging method for global time steps can be used to efficiently accelerate the solution process. Recently, an implicit time-accurate dual time-stepping method (see Jameson (1991)) which solves the governing equations via an explicit time-integration in a pseudo time has been implemented. With this method, all acceleration methods that apply to steady state simulations can be used to increase the convergence rate in the pseudo-time integration. The message passing interface (MPI) was used to parallelize the solver in an ad hoc manner. The grid block based parallelization takes advantage of the multiblock structure of the solver.

Turbine Flow Simulation

Two sets of computations have been carried out in order to account for the two different operating conditions which were used in the experiments. Each set consisted of simulations with two different grid densities and efficiency studies of two distinct acceleration techniques for unsteady flow simulations: dual-time stepping with time-accurate multigrid and a pure explicit time-consistent multigrid algorithm. The coarse grid discretization consisted of a total 293,523 nodes, i. e. roughly 100,000 nodes per blade row, and the tip clearance gap was modelled with 2925 grid points. For the fine grid simulations the computational domain was discretized with 2,116,941 nodes, i. e. compared to the coarse grid the number of grid points was increased by a factor of about 2 in each spatial direction (e. g. $137 \times 73 \times 65$ nodes in the second stator. Here the number of nodes in the rotor tip gap amounted to 31,185. For the fine grid simulation the dimensionless wall distance was $y^+ < 7$ for the two stators $y^+ < 5$ for the rotor. A three-dimensional view of the coarse grid on the hub and the blade surfaces is shown in Fig. 4. Results of preceeding steady-state simulations were used as initial conditions for the unsteady simulations. It was found that after seven blade passing periods the transient disturbances resulting from these – for unsteady simulations – inconsistent

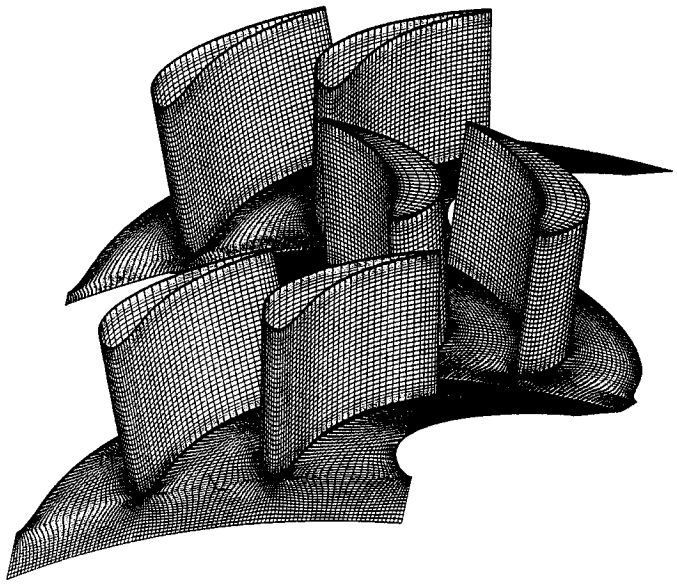

Figure 4: Computational grid for the turbine (coarse discretization)

initial conditions have diminished sufficiently. So all the results shown below are extracted from the flow field during the eighth or later blade passing period after the start of the unsteady simulation.

The coarse grid simulations were carried out on a 333 MHz single processor DEC Alpha workstation. With the explicit time-consistent multigrid method each blade passing period took about 10:52 hours of CPU time, i. e. 88 μs/(time step $\times$ node). The implicit dual-time-stepping method using three level full multigrid cycles for the pseudo-time integration needed about 22:40 hours per period (124 μs/(pseudo time step $\times$ node)). Also the memory requirement was higher for the dual-time stepping method than with the pure explicit algorithm (91 MB vs. 64 MB, 32 bit per word).

The parallel version of the code was used for the fine grid simulations which were carried out on the NEC SX-4 vector-parallel supercomputer at the HPC center of the University of Stuttgart. Using 4 of the 32 vector processors, each blade passing period took about 7:20 hours in real time with the dual-time stepping method and a five level multigrid cycle for each explicit iteration in the pseudo time (5.8 μs/(pseudo time step $\times$ node)). For each period 100 implicit time steps have been used. Here the memory requirement was 1.34 GB (64 bit per word). The concurrent processor performance was more than 1.1 GFlop/s with a parallel speed-up greater than 3 for the pure calculation and going down to 0.91 GFlops/s during the last blade passing period due to the large amount of i/o operations. With this fine discretization, the explicit multigrid method proved to be not a quarter as efficient as the dual-time stepping method. The simulations with the explicit algorithm were cancelled as it turned out that more than 7,500 iterations per period would be required in order to get the calculation stable.

An example of the influence of the different grid densities on the numerical results is shown in Fig. 5. Plotted is the instantaneous entropy distribution in the second stator at mid-span at identical stator/rotor positions. The left figure shows the result for the coarse grid simulation whereas the fine grid result is depicted on the right. Looking at the shape of the contours it becomes obvious, that a lot of details are missing in the coarse grid results which are captured by the fine grid.

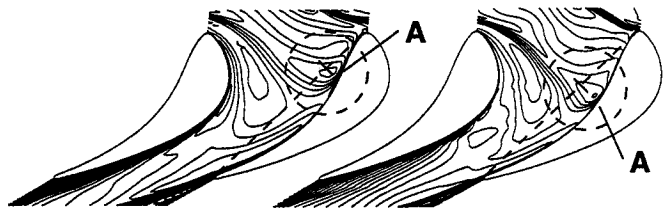

Figure 5: Instantaneous entropy distribution in the second stator at mid-span at identical rotor/stator positions (left: coarse grid simulation, right: fine grid simulation)

Detail A shows the differences in the rotor wake/boundary layer interaction and wake convection behaviour. Remarkable are the different shapes and locations of the local extrem values in the two results. The extrem value in the coarse grid simulation is located at about 25 % of the blade chord whereas the corresponding extremum of the fine grid simulation is at about 35 % of the chord. This means, that the two simulations show a noticable phase shift in the time-dependent behaviour and appearance of phenomena associated with this quantity. Another simulation with an even finer grid would be necessary in order to prove that the fine grid results are already reasonably grid independent. All the results presented below are taken from the fine grid simulations.

RESULTS AND DISCUSSION

All presented figures of cross flow sections are rear views as seen from downstream. The pitchwise flow angle α starts at circumferential direction and its counterclockwise rotation is positive, see Fig. 2. Spanwise flow angles γ have positive values when directing to the casing. Thus a steady three-dimensional flow vector is given as

$$\vec{c}_{\text{loc}} = f(c, \alpha, \gamma)_{\text{loc}} \tag{1}$$

and a three-dimensional time-dependent flow vector as

$$\vec{c}(t)_{\text{loc}} = f(c(t), \alpha(t), \gamma(t))_{\text{loc}} \tag{2}$$

A secondary flow vector is the difference vector between the local flow vector and an averaged flow vector. The latter is calculated using the total local velocity $|\vec{c}|$, the radially averaged yaw angle $\bar{\alpha}^r$ and the circumferentially averaged pitch angle $\bar{\gamma}^\varphi$:

$$\vec{c}_{\text{sec}} = \vec{c}_{\text{loc}} - \vec{c}_{\text{avg}} \tag{3}$$

with

$$\vec{c}_{\text{avg}} = f(|\vec{c}|, \bar{\alpha}^r, \bar{\gamma}^\varphi) \tag{4}$$

Unsteady flow behind the rotor

Second stator inlet flow is equivalent with rotor exit flow in the absolute frame. To understand the unsteady flow behaviour in and behind the second stator it is therefore necessary to discuss the results at the rotor exit in frame of reference of the second stator, i. e. in the absolute frame.

The time-dependent secondary flow field in the axial gap between the rotor and the second stator is shown in Fig. 7 for eight different rotor/stator positions. A key for the numbers used to mark flow phenomena is given in Table 1. The arrows represent the components of the secondary flow vector viewed from the downstream direction which is given by the design angle at outlet of the blade row. This is valid for all following figures showing secondary flow vectors. Also, the description of the distinct flow features is – if not noted otherwise

No.	Description
1	Casing passage vortex
2	Hub passage vortex
3	Trailing edge vortex
4	Tip clearance vortex
5	Influence due to first stator
6.1	Rotor casing passage vortex
6.2	Rotor hub passage vortex
6.3	Rotor trailing edge vortex
7	Combi vortex (second stator)

Table 1: Reference of secondary flow figures

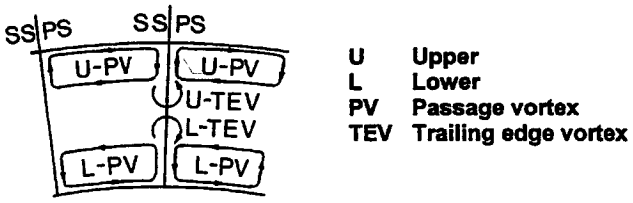

Figure 6: Development of trailing edge vortices

– relative to the domain of interest of the experiments. For easier orientation, this domain of interest is also shown in the numerical results, where its approximate boundaries are indicated with dashed lines.

Close to the hub a distinctive flow from pressure side to suction side, forming the lower part of the hub passage vortex, can be observed. At approximately 75 % span flow in the opposite direction from suction to pressure side forms the lower side of the casing passage vortex. Behind the trailing edge slightly above midspan the upper and lower trailing edge vortices develop from the shear layers in the wake some distance behind the cascade. The mechanism of the formation of the trailing edge vortices is illustrated in the sketch in Fig. 6. Below it will be shown that especially the upper trailing edge vortex plays an important role in the interaction between rotor and second stator.

Except for the time indices TI 1, TI (, and TI 17 the casing passage vortex (1) and hub passage vortex (2) are the dominating flow features (Fig. 7). The flow field shows biggest differences between TI 1 and TI 33. The latter leaves an overall balanced impression of a typical blade exit flow containing the distinctive passage vortices. On the other hand at TI 1 a flow distortion due to the first stator (5) appears in the area of the hub passage vortex. The formerly rotational sense in the counterclockwise direction is disturbed and at TI 17 only a diagonal inward directed slanted structure is left. Together with the appearance of the described distortion at approximately 70 % span another vortex (3) can be seen rotating in the counterclockwise direction as well. Its upper part seems to go together with the lower part of the casing passage vortex. Location and rotational sense conclude that this structure is the upper trailing edge vortex of the just passing rotor blade. At TI 17 the same structure can be detected. The extension of the trailing edge of the corresponding blade can be recognized in form of the effects of the wake on the flow. Nearly all flow vectors directing from suction to pressure side undergo a strong turning radial upwards forced by the high pressures induced on the pressure side of the blade. Note that this cross flow section is located 8 mm downstream of the trailing edge of the rotor. Hence, at this location, there are already strong mixing processes between the wake and the main flow taking place. Comparing the experiments with the simulation, it can be stated that all the major flow phenomena and their locations are in reasonably good agreement except for the casing passage vortex which in the experiments is found to be more distinct than in the simulation. When doing such comparisons, it should be kept in mind that these are comparisons of time-dependent secondary flow vectors, i. e. these are just the temporal fluctuations of values that remain when subtracting two quantities of equal order of magnitude.

Unsteady flow within the passage of the second stator

This section discusses the experimental and numerical results in some selected cutting planes within the passage of the second stator. Refer to Fig. 3 for the location of the measurement planes. The time-dependent secondary velocities at plane 14, which is located a short distance downstream of the inlet of the passage, and at plane 0, which is equivalent to the outlet plane of the second stator are shown in Figs. 8 and 9. Time-dependent absolute Mach number perturbations at 24 %, 50 %, and 73 % of the blade span are presented in Figs. 10 to 12. Plots depicting the time-dependency of the pitchwise flow angle perturbation at 24 % and 50 % of the span are shown in Figs. 13 and 14. Instantaneous radial flow angle distributions at 50 % and 73 % span are presented in Figs. 15 and 16.

Comparing secondary flow in plane 14 (stator passage, Fig. 8) and secondary flow at rotor exit (Fig. 7) all vortices which have been found in the rotor exit flow are detectable in plane 14 as well. Starting at TI 1 and moving with time the first full vortex structure recognizable in both the experimental and numerical results is found at TI 17 at about 30 % span. Counterclockwise rotational sense and location point out that it is the rotor hub passage vortex (6.2). At about 85 % span, a strong crossflow from the right to the left can be seen. TI 25 and TI 33 show this crossflow as the lower part of the clockwise rotating casing passage vortex of the rotor (6.1). During the circumferential movement from TI 17 to TI 33 a remarkable change in the radial position of 6.1 can be noticed. Moving further on with time both vortices have partly been chopped by the stator vane at TI 41, at TI 57 they are not longer detectable from the experimental results, wheras the simulation shows that this vortex is pushed against the stator blade suction side, where it takes as long as until TI 9 till it is completely dissolved and the cycle starts over again. The trailing edge vortex (6.3) is not as distinctive as in Fig.7 but careful observation shows its presence all the time between TI 1 and TI 41. The simulation shows quite a good agreement in the motion and the strength of the upper trailing edge vortex. From TI 17 to TI 33 another vortex structure can be recognized from the prediction in the lower right corner next to the rotor hub passage vortex. Its rotational sense and location identify it as the lower trailing edge vortex.

Figure 9 presents time-dependant secondary flow in the outlet of the passage of the second stator (plane 0). The rotor vortex system consisting of 6.1, 6.2 and 6.3 is still detectable and appears clearly with the rotor casing passage vortex (6.1) and the trailing edge vortex (6.3) at TI 17. The numerical results show a dominating vortex (6.3) a bit earlier at TI 9. The rotor hub passage vortex seems just to appear bottom right at about 15 % span at TI 17. When the rotor has moved 12.5 % of its pitch, all three vortices can be seen on the left hand side of figure TI 25. Bottom right in this figure of the experimental results, the stator hub passage vortex can be identified due to its clockwise rotational sense and radial position close to the hub. The simulation predicts its appearance somewhat later. It is clearly recognizable at TI 41. The circumferential position is not, as one would expect, close to the suction side. Unsteady interaction between rotor hub passage

vortex (6.2) and stator hub passage vortex (2) has removed the latter from its usual position.

The following figures (Figs. 10 to 16) shows selected flow quantities for azimuthal cutting planes at three different spanwise locations (i. e. 24 %, 50 %, and 73 % of the span). Plotted is the perturbation of the absolute Mach number and the pitchwise flow angle as well as the unsteady radial flow angle. The perturbation is calculated as the difference between unsteady and time-averaged values for each point, e.g. $Ma' = Ma_{uns} - Ma_{avg}$. In all figures the darker shaded areas correspond to values smaller than the time-averaged values. The predicted results are plotted to the right hand side of the corresponding experimental results. The solid line in the plots of the numerical results indicates the measured region.

The low Mach number regions show the path of low energy material (associated with the rotor wake) within the stator passage. Fig. 10 shows top left at TI 49 a just incoming rotor wake. Another dark area can be seen further downstream. It determines the location of the wake which entered the stator passage one blade passing period earlier. At TI 1 (Fig. 12 three of those zones are detectable: top right, top left and at passage exit when refering to the common domain of interest in the experiments and calculations. Following the time indices the movement of this wake fluid in the stator passage can be traced. So the top right area needs about 1.75 blade passing periods between entering and leaving the stator passage. At midspan, Fig. 11 the time-dependent behaviour is similar, but the shapes of the low Mach number regions are different. Reason for this is the pressure gradient which is much stronger in pitchwise direction and which forces the low energy material to move towards the suction side of the passage. A very good agreement between the measured and predicted values of this time-dependent behaviour can be stated for the shape of the contours as well as for the magnitude.

Figs. 13 and 14 depict the perturbation of the pitchwise flow angle α' and thus corresponds to the motion of the low energy fluid as just discussed for the Mach number. In areas of low Mach number perturbations this yaw angle perturbation is negative as well and shows negative incidence, corresponding with a decreased loading of the stator blade row. Remarkable are the different locations at the same time indices, comparing Figs. 13 and 14 at TI 1. At 24 % span the wake fluid has just entered the passage, whereas at midspan the wake fluid is already in the vicinity of the maximum camber of the blade. Different speeds at different radii are responsible for this phenomena.

Little change with time shows the spanwise flow angle, see Figs. 15 and 16. Only in the first quarter of the stator passage (streamwise) the rotor influence is clearly detectable. The agreement between the experiments and the simulation is good at the mid-span location whereas it can be stated to be excellent at 73 % of the span. Please note, that the quantity compared here – unlike the perturbations discussed above – is the flow angle itself and not its fluctuation. This is remarkable, because good agreement in the fluctuations does not necessarily come along with a good agreement of the quantity itself.

Unsteady flow behind the second stator

Time-dependent secondary flow behind the second stator is shown in Fig. 17 at eight different rotor/stator positions. The plane of measurements is located 8 mm behind stator outlet in the axial direction. In the experiments at TI 1 several vortex structures can be distinguished. The origin of each vortex can be revealed by taking into account the rotational sense of each vortex, its location, and its time-dependent behaviour. The vortex (6.1) close to casing and suction side of the stator blade rotates in the clockwise direction whereas the weak vortex structure (1) on the right hand side rotates counterclockwise. This is the rotational sense of the stator casing vortex but the location (casing, pressure side) does not fit. Observing the top right corner of TI 33, TI 41, ... TI 1, it can be seen that a structure rotating counterclockwise (as the casing stator passage vortex) appears. It is distinctive at the beginning (TI 33) and diminishing with rotor movement until the weak vortex structure already mentioned appears (TI 1). At TI 9 the stretched vortex (6.1) has disappeared and been replaced by the casing passage vortex (1) of the second stator.

Considering the structure of the rotor exit flow in the absolute frame, the radial inward directing and stretched looking vortex (6.1) must be the rotor casing passage vortex. At TI 33, at the same location, this vortex has the same structure and rotational sense as its counterpart behind the rotor (see Fig. 7). Its sudden appearance at TI 33, the change of its shape with time followed by complete disappearance points clear to a rotor vortex chopped by the stator vanes.

A similar but more complex vortex system (2, 6.2, 6.3) can be seen bottom left at TI 1, filling nearly half the figure. It obviously consists of three different vortices, where the one located bottom left (6.2) shows only a bit more than half of the usual circular shape. Looking at the rotational sense it is found that the two vortices on top of each other (6.3, 6.2) do have the same rotational sense (counterclockwise). The third vortex (2) rotates clockwise. Moving with the rotor to TI 9 this structure becomes very weak but is still detectable. Later on at TI 25 the hub passage vortex (2) is clearly to recognize close to the suction side. Following the way from TI 1 to 25 it is found that structure (2) has moved from pressure to suction side and thus must be the hub passage vortex of the second stator.

Bottom in the right third of the figure at TI 25 a new vortex structure rotating clockwise seems to appear. Comparing this with TI 33 the small hub passage vortex has been removed completely by the sudden appearance of a large vortex structure (6.2) rotating in the opposite direction. The sudden appearance and the rotational sense lead to the conclusion that this vortex is originated in the rotor and identical with the rotor hub passage vortex. Left of the center of the figure (TI 33) a vortex (6.3) which is also rotating counterclockwise can be seen. Rotational sense, location and the observations within the passage of the second stator indicate that this is the upper trailing edge vortex coming from the rotor exit. It is also detectable that there is some transport of material from the lower vortex (6.2) to the upper vortex (6.3). The amplification of two vortices leads to the huge vortex (7) which can be seen at TI 49 filling more than half the area representing this figure. TI 57 shows bottom right a diagonally inward directed new vortex structure (2) which is barely detectable at TI 49. It causes an indentation in the vortex structure (7). This disturbance together with the diminishing rotor hub passage vortex leads to the disintegration of structure (7) as observable at TI 1. The measurements and simulation show a good agreement in the overall structure of the vortex systems and their time-dependency. Some discrepancies can be observed in the locations and relative strength of the vortices.

Finally, an overall impression of the unsteady flow throughout the machine is given in Fig. 18. It depicts the computed instantaneous entropy distribution at mid-span for three adjacent blade-to-blade passages.

CONCLUSIONS

To investigate unsteady stator/rotor/stator interaction in a 1.5 stage axial flow turbine measurements in the axial gaps and within the passage of the second stator have been performed. Three-dimensional

Navier-Stokes simulations which include tip clearance modeling and blade row interaction with the real blade counts of the three blade rows have been carried out. Experimental and numerical results of the time-dependent secondary flow fields and other flow properties have been presented in this paper for several cutting planes throughout the domain of the second stator. Results lead to the following conclusions:

- Rotor exit flow shows influence of the exit flow of the first stator at several rotor/stator positions.
- Typical passage vortices have been found to be the dominating flow features in the rotor exit flow. Trailing edge vortices were detected at the rotor exit.
- Rotor passage vortices and rotor trailing edge vortices have been tracked inside the passage of the second stator.
- All vortices leaving the rotor passage strongly influence the flow within and behind the second stator.
- Highly three-dimensional unsteady effects are main features in the flow behind the second stator. They would define the inlet conditions of a second rotor.
- Rotor tip clearance flow effects were found to be small and not significant for the second stator flow.
- ITSM3D is able to predict most of the unsteady phenomena found in the experiments.
- A grid dependent phase shift is found in the numerical results. This is an important behaviour which significantly influences the time-accuracy of unsteady multi-blade row calculations.
- Further work is necessary to prove grid independency for unsteady flow simulations.
- Overall agreement between numerical and experimental results for time-dependent quantities is promising and encourages further investigations in order to perform a thorough code validation for such a complex three-dimensional unsteady internal flow.
- Once this validation is achieved the predicted flow field can be analized with todays post-processing capabilities (e. g. virtual reality animation) to further improve the understanding of the unsteady flow behaviour in multistage turbomachinery without the difficulties related to unsteady data acquisition.
- Further analysis of the large amount of experimentally and numerically obtained data with focus on other aspects of unsteady turbine flow will be addressed in a future paper.

Improving the knowledge on unsteady flow physics and the loss production mechanisms in turbomachines will finally help to develop methods for designing more efficient blades.

ACKNOWLEDGEMENT

The experimental work was supported bei the Forschungsvereinigung Verbrennungskraftmanschinen e. V. (FVV) which is gratefully ackowledged. The authors appreciate the funding of the numerical research by the Deutsche Forschungsgemeinschaft (DFG).

REFERENCES

Binder, A., Förster, W., Kruse, H. and Rogge, H., 1985, "An Experimental Investigation into the Effect of Wakes on the Unsteady Turbine Rotor Flow," J. Engrg Gas Turb. Power (Trans. ASME), vol. 107, pp. 458-466.

Dawes, W. N., 1994, "A Numerical Study of the Interaction of a Transonic Compressor Rotor Overtip Leakage Vortex with the Following Stator Blade Row," ASME 94-GT-156.

Eulitz, F., Engel, K., Gebing, H., 1996,"Numerical Investigation of the Clocking Effects in a Multistage Turbine," ASME 96-GT-026.

Gallus, H.E., Zeschky, J. and Hah, C., 1994, "Endwall and Unsteady Flow Phenomena in an Axial Turbine Stage," ASME 94-GT-143.

Giles, M. B., 1988, "Non-Reflecting Boundary Conditions for the Euler Equations," Tech. Rep. TR-88-1, MIT CFD Laboratory.

Giles, M. B., 1991, "UNSFLO: A Numerical Method for the Calculation of Unsteady Flow in Turbomachinery," GTL Rep. No. 205, MIT Gas Turbine Laboratory.

Gregory-Smith, D. G., 1995, "3D Flow Simulation in Turbomachinery – The ERCOFTAC Seminar and Workshop III, January 1994," VDI-Berichte 1185, pp. 35–49.

Hah, C., Copenhaver, W.W. and Puterbauch, S.L., 1993, "Unsteady Aerodynamic Flow phenomena in a Transonic Compressor Stage," AIAA-93-1868.

Hall, E. J., 1997, "Aerodynamic modelling of Multistage Compressor Flowfields - Part1: Analysis of Rotor/Stator/Rotor Aerodynamic Interaction," ASME 97-GT-344.

He, L., 1996, "Time-Marching Calculations of Unsteady Flows, Blade Row Interaction and Flutter," VKI-LS 1996-05.

Hodson, H. P., Dawes, W. N., 1996, "On the Interpretation of Measured Profile Losses in Unsteady Wake-Turbine Blade Interaction Studies," ASME 96-GT-494.

Hunter, I. H., 1982, "Endwall Boundary Layer Flows and Losses in an Axial Turbine Stag," J. for Engineering Power (Trans. ASME), Vol. 104, pp. 184-193.

Jameson, A., Schmidt, W., Turkel, E., 1981, "Numerical Solutions of the Euler Equations by Finite Volume Methods Using Runge Kutta Time-Stepping Schemes," AIAA 81-1259.

Jameson, A., 1991, "Time Dependent Calcuations Using Multigrid, with Applications to Unsteady Flows Past Airfoils and Wings", AIAA-91-1596.

Joslyn, H. D., Dring, R. P. and Sharma, O. P., 1983,"Unsteady Three-Dimensional Turbine Aerodynamics", Journal for Engineering Power (Trans. ASME), Vol. 105, pp. 322-331.

Joslyn, D. and Dring, R., 1992,"Three-Dimensional Flow in an Axial Turbine: Part 1 - Aerodynamic Mechanisms; Part 2 - Profile Attenuation", J. of Turbomachinery (Trans. ASME), Vol. 92, pp. 61–78.

Jung, A. R., Mayer, J. F., Stetter, H., 1996, "Simulation of 3D-Unsteady Stator/Rotor Interaction in Turbomachinery Stages of Arbitrary Pitch Ratio," ASME 96-GT-69.

Merz, R., Krückels, J., Mayer, J. F., Stetter, H., 1995, "Calculation of Three-Dimensional Viscous Transonic Turbine Stage Flow Including Tip Clearance Effects," ASME 95-GT-76.

Morphis, G. and Bindon, J.P., 1994, "The Flow in a Second Stage Nozzle of a Low Speed Axial Turbine and its Effect on Tip Clearance Loss Development," ASME 94-GT-145.

Sharma, O. P., Butler, T. L., Joslyn, H. D. and Dring, R. P., 1985, "Three-Dimensional Unsteady Flow in an Axial Flow Turbine," Jet Propulsion, Vol. 1, No. 1, pp. 29-38.

Sharma, O. P., Renaud, E., Butler, T. L., Milsaps, K., Dring, R. P. and Joslyn, H. D., 1988, "Rotor-Stator Interaction in Multi-Stage Axial-Flow Turbines," AIAA-88-3013.

Valkov, T. and Tan, C.S., 1993, "Control of the Unsteady Flow in a Stator Blade Row Interacting with Upstream Moving Wakes," ASME 93-GT-23.

Walraevens, R. E., Gallus, H. E., 1996, "Stator-Rotor-Stator Interaction in an Axial Flow Turbine and its Influence on Loss Mechanisms," AGARD-CP-571, pp. 39/1–39/14.

Yamamoto, A., Mimura, F., Tominaga, J., Tomihasa, S., Outa, E. and Matsuki, M., 1993, "Unsteady Three-Dimensional Flow Behavior due to Rotor-Stator Interaction in an Axial-Flow Turbine", ASME 93-GT-404.

Zeschky, J. and Gallus, H. E., 1993, "Effects of Stator Wakes and Spanwise Nonuniform Inlet Conditions on the Rotor Flow of an Axial Turbine Stage," J. of Turbomachinery (Trans. ASME), Vol. 115, pp. 128-136.

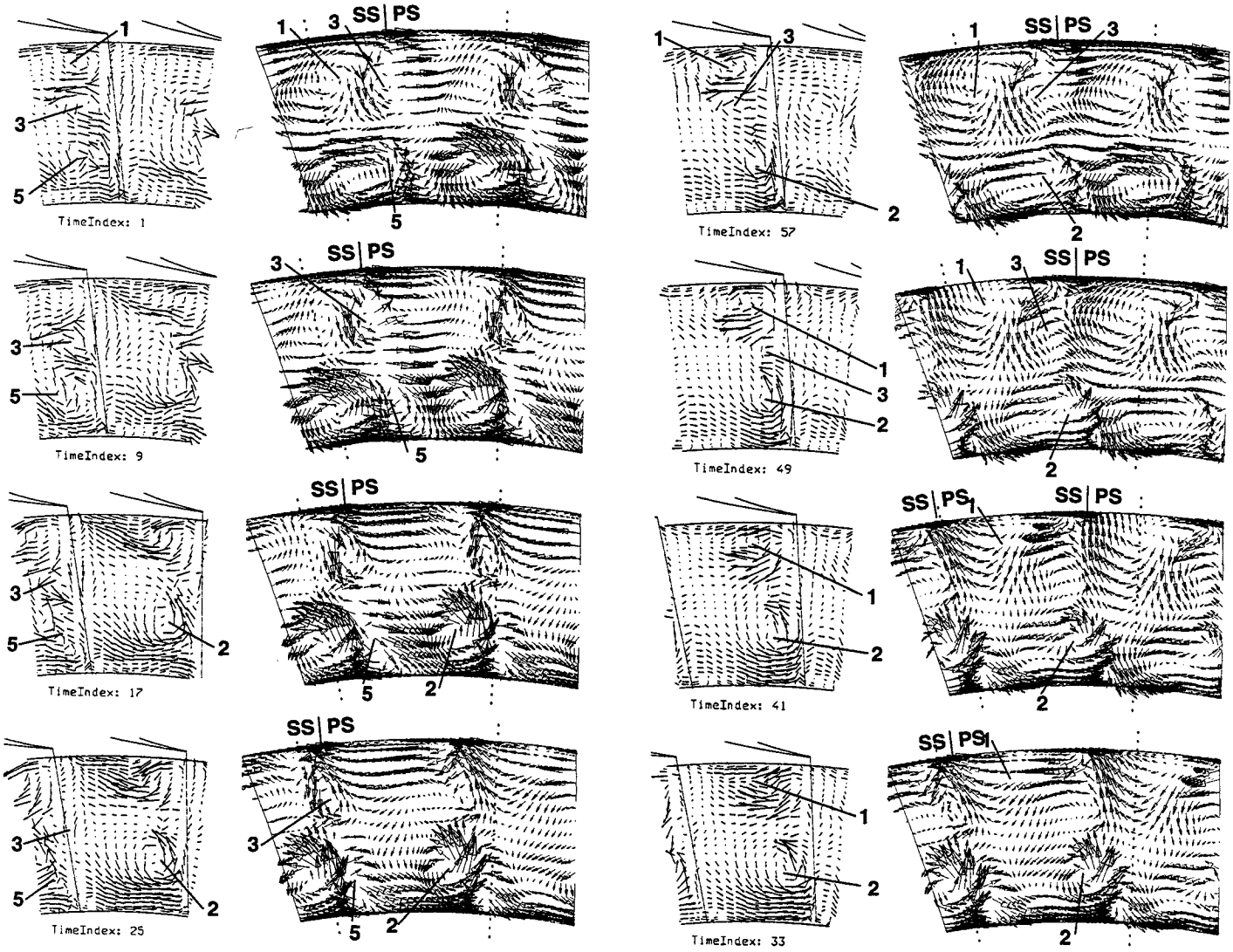

Figure 7: Time-dependent secondary flow field at rotor exit in the absolute frame (left: experiment, right: simulation)

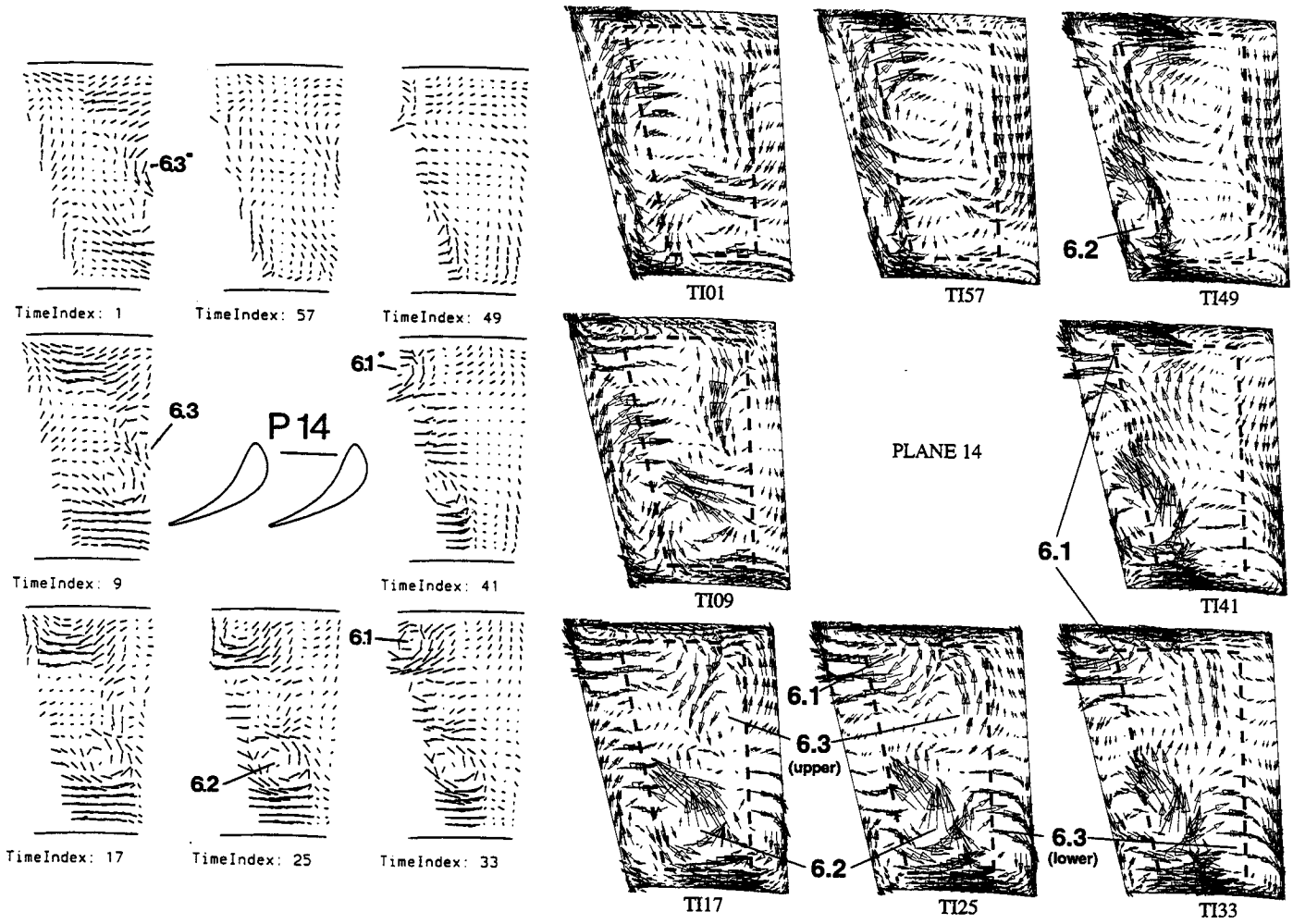

Figure 8: Time-dependent secondary flow within the passage of the second stator close to inlet – plane 14 (* – chopped vortex, left: experiment, right: simulation)

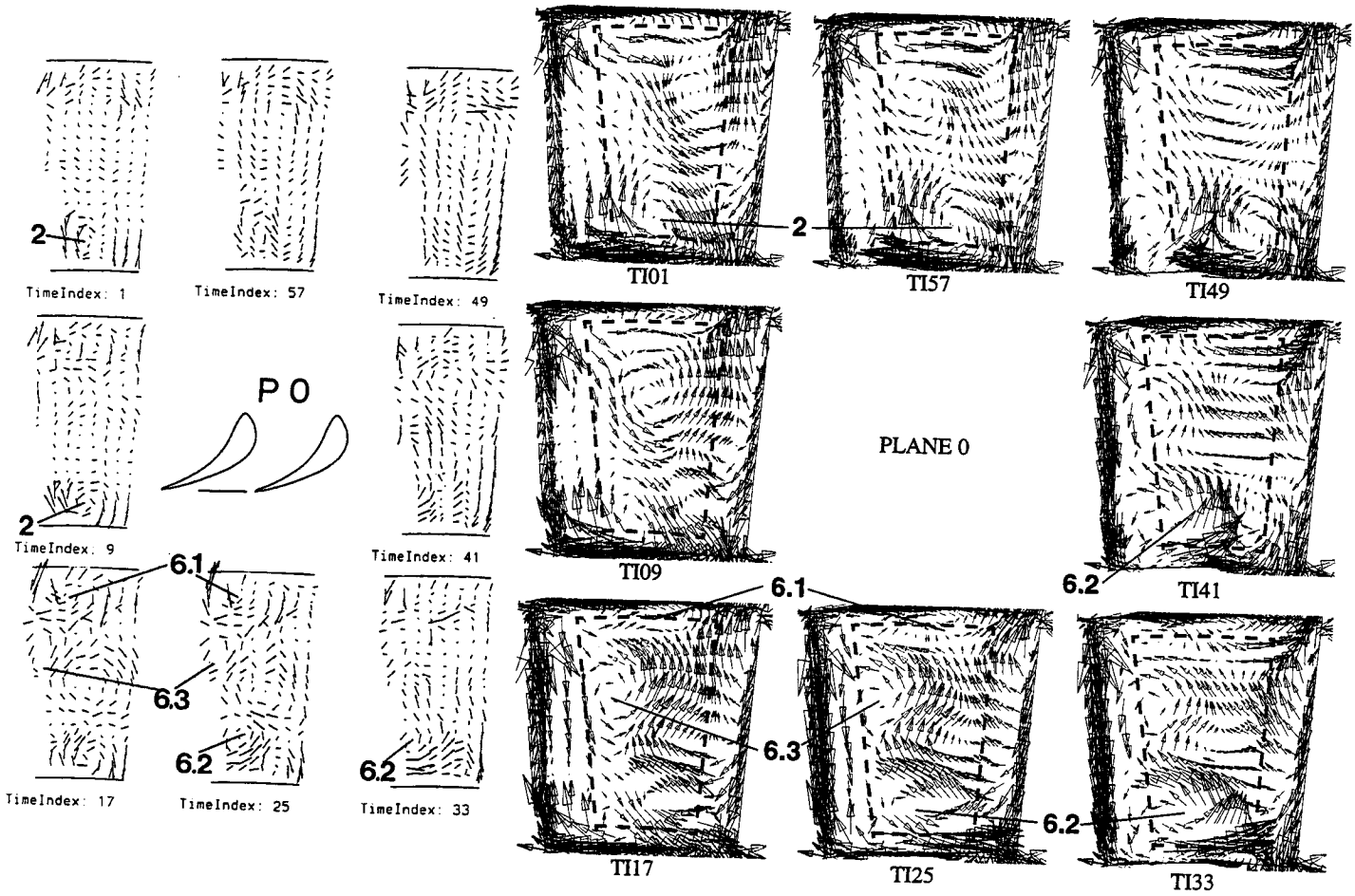

Figure 9: Time-dependent secondary flow at the exit of the passage of the second stator – plane 0 (left: experiment, right: simulation)

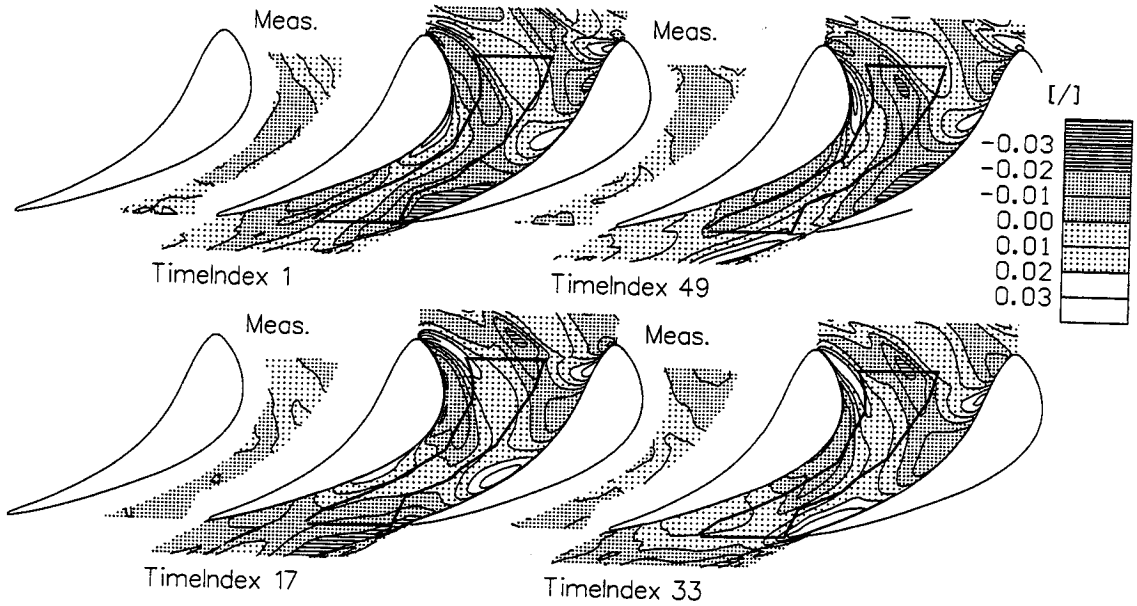

Figure 10: Mach number perturbation at 24 % span (left: experiment, right: simulation)

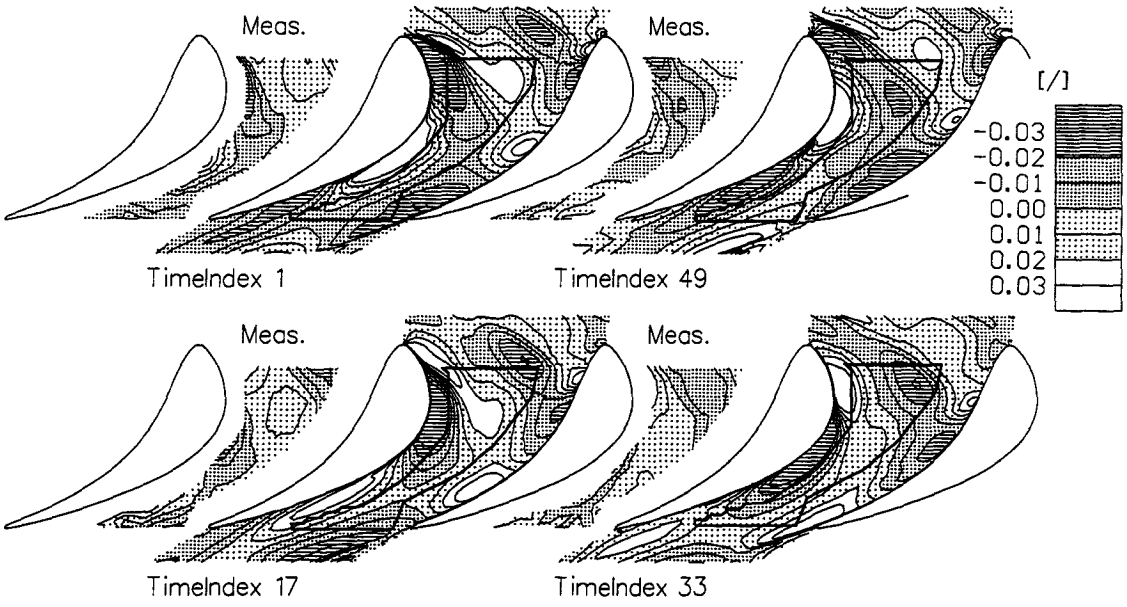

Figure 11: Mach number perturbation at mid-span (left: experiment, right: simulation)

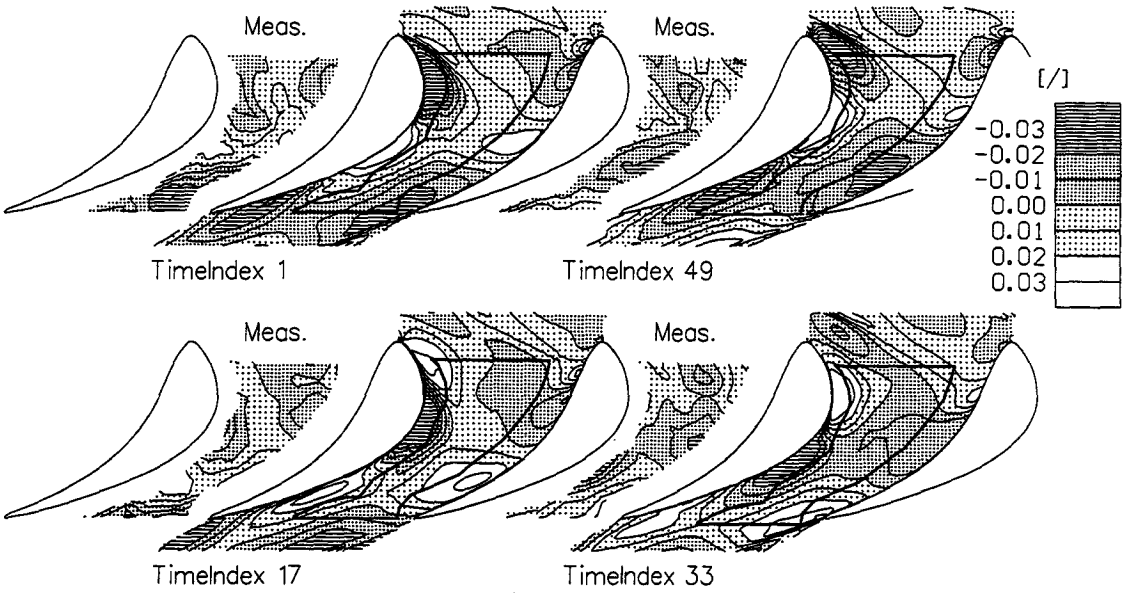

Figure 12: Mach number perturbation at 73 % span (left: experiment, right: simulation)

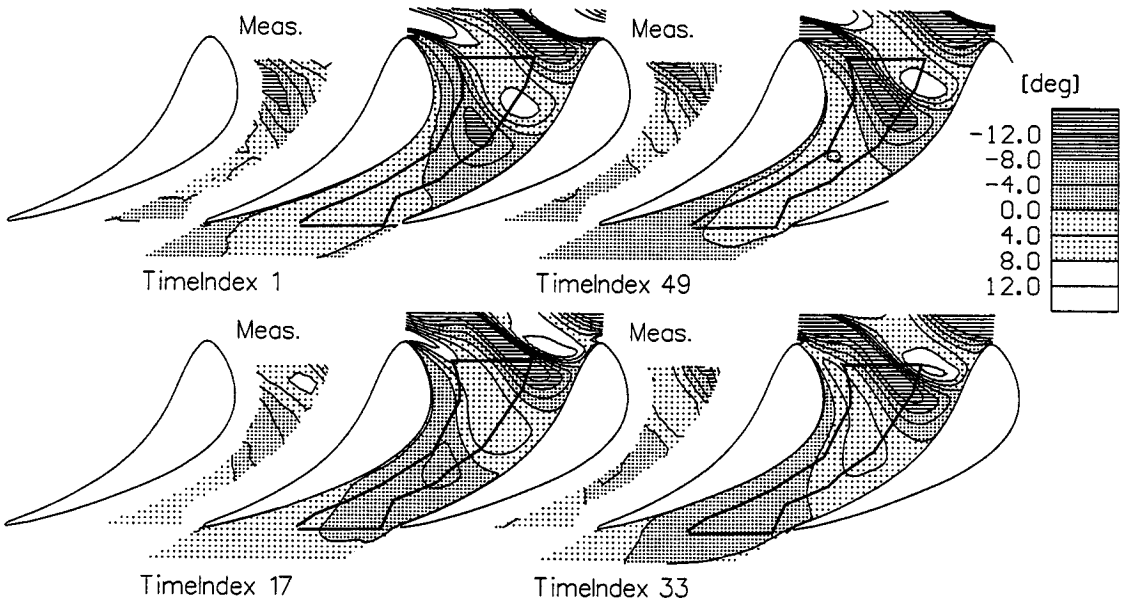

Figure 13: Perturbation of pitchwise flow angle α at 24 % span (left: experiment, right: simulation)

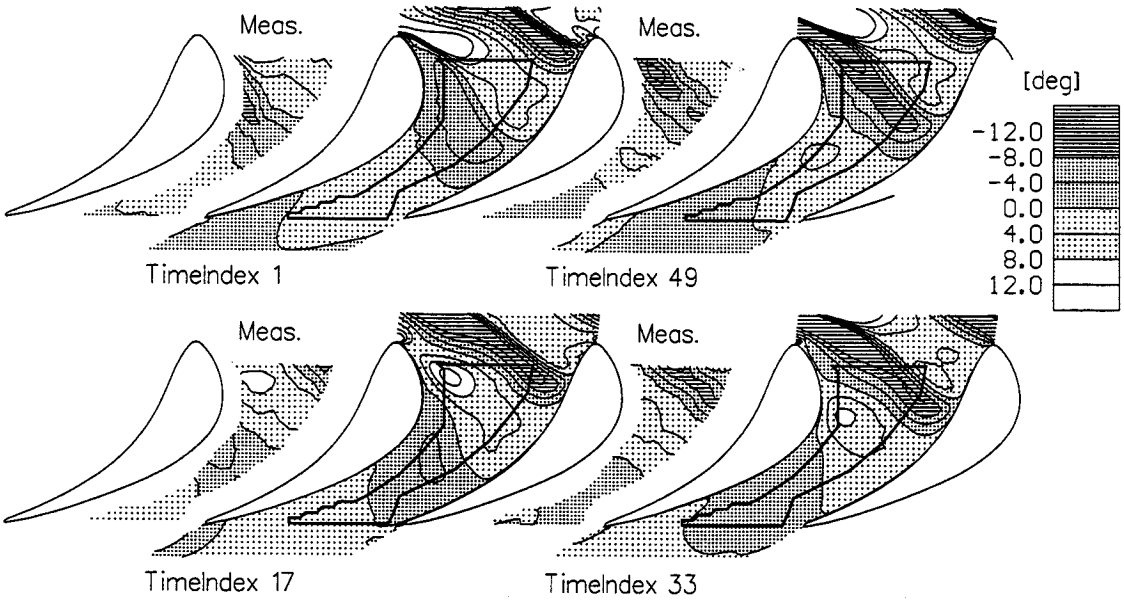

Figure 14: Perturbation of pitchwise flow angle α at mid-span (left: experiment, right: simulation)

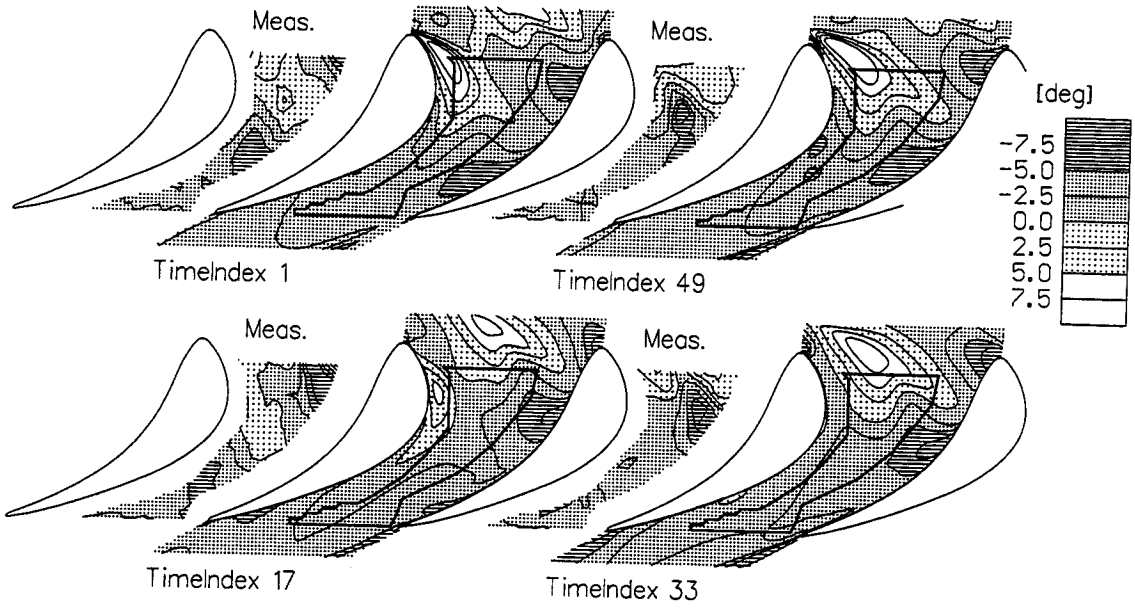

Figure 15: Time-dependent radial flow angle γ at mid-span (left: experiment, right: simulation)

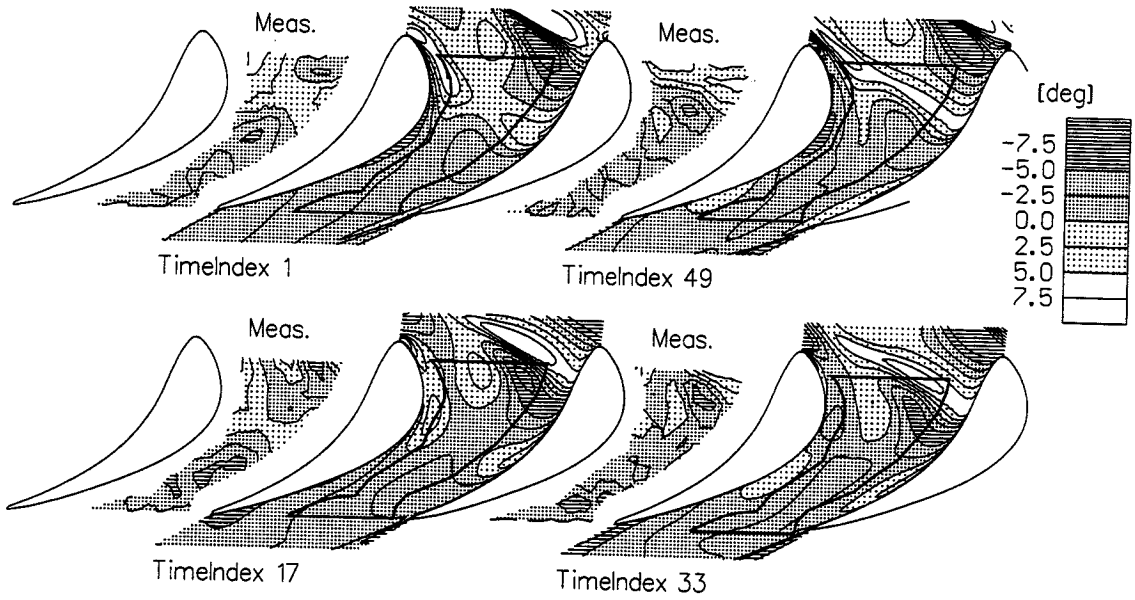

Figure 16: Time-dependent radial flow angle γ at 73 % span (left: experiment, right: simulation)

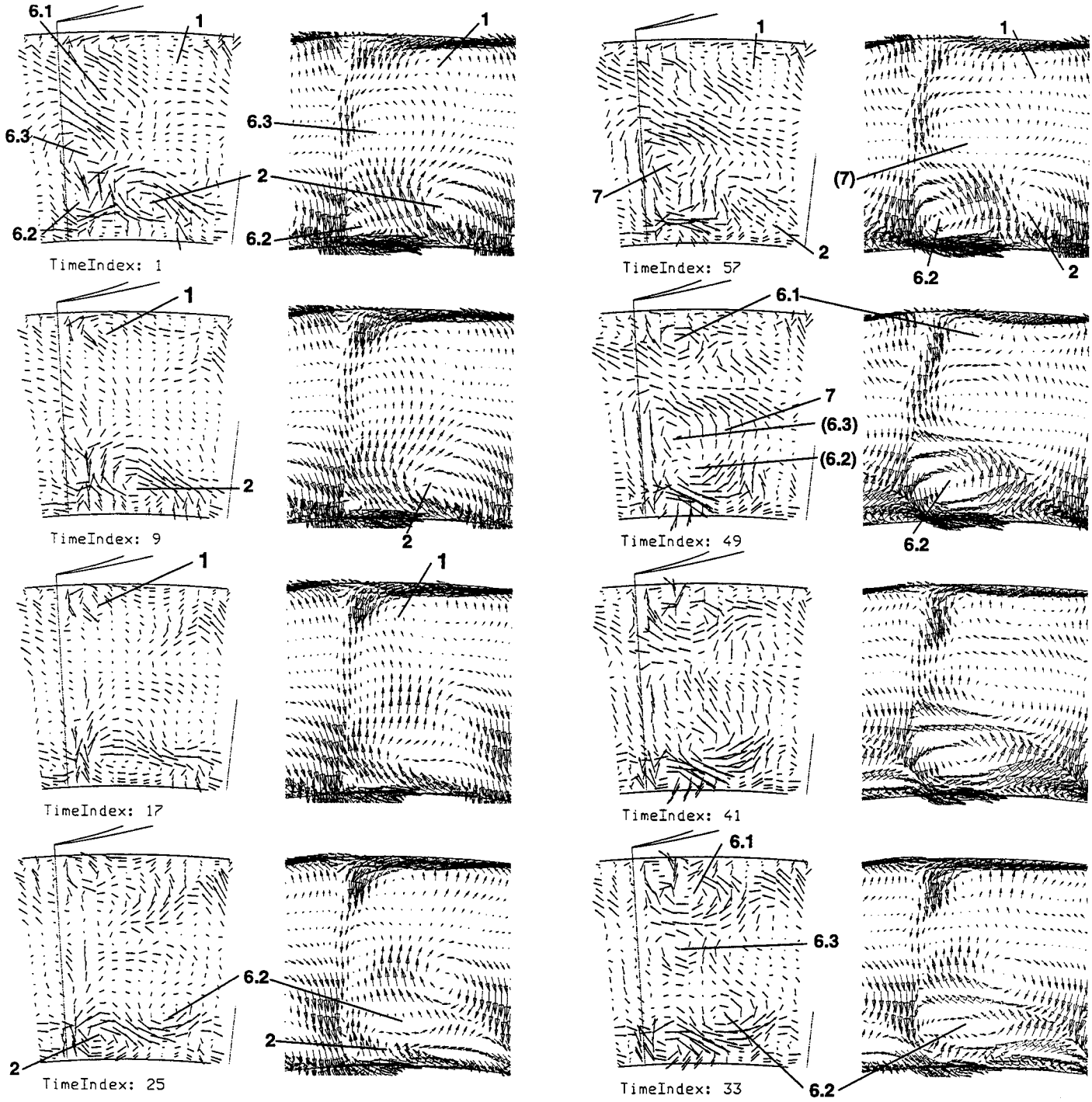

Figure 17: Time-dependent secondary flow field behind the second stator (left: experiment, right: simulation)

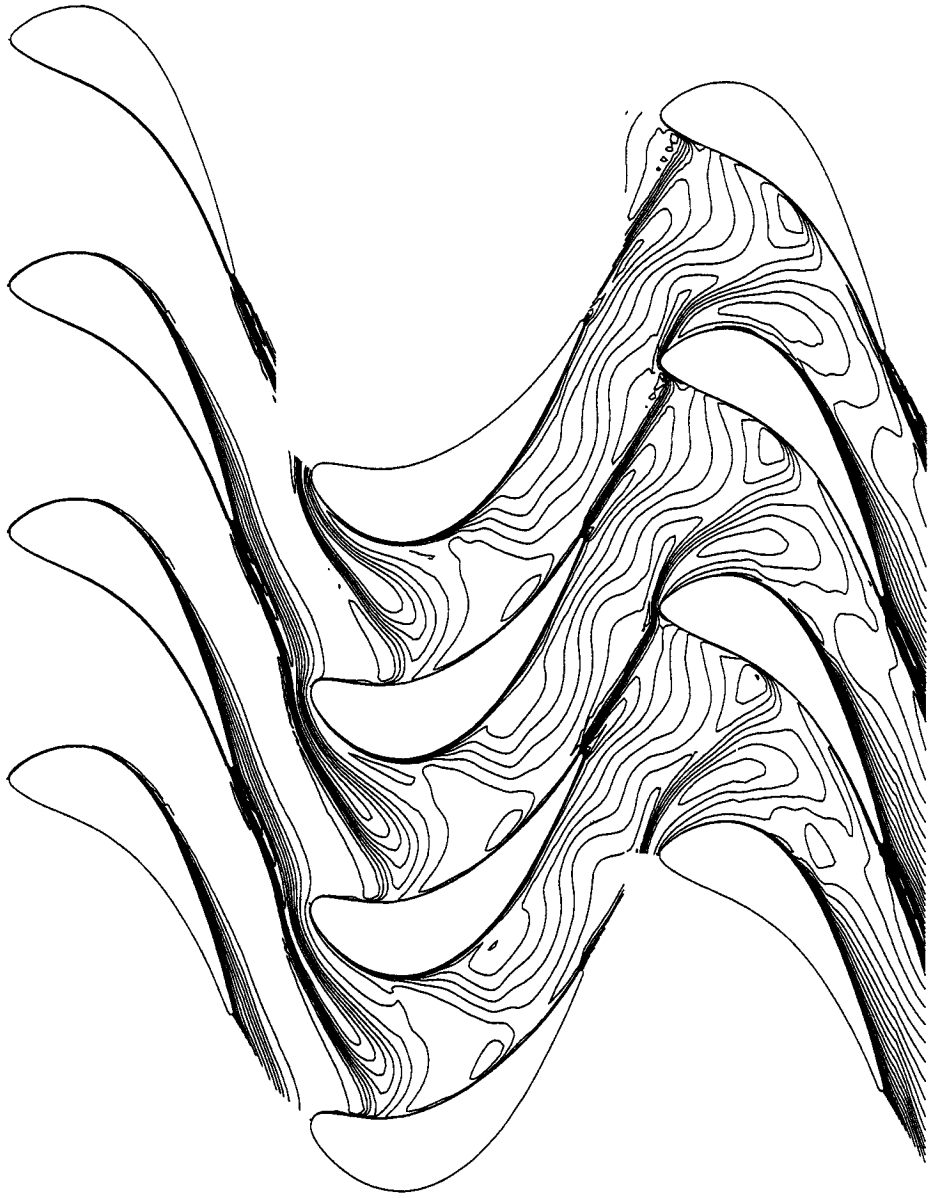

Figure 18: Instantaneous entropy distribution in the turbine at mid-span (simulation)